

pubs.acs.org/acsaelm Article

Solution-Processed Ternary Perovskite-Conjugated Polymer Photodetector with a Photoresponse up to 1200 nm

Lening Shen, Xiyao Zhang, Lei Liu, Hussain Sawwan, Tao Zhu,* and Xiong Gong*



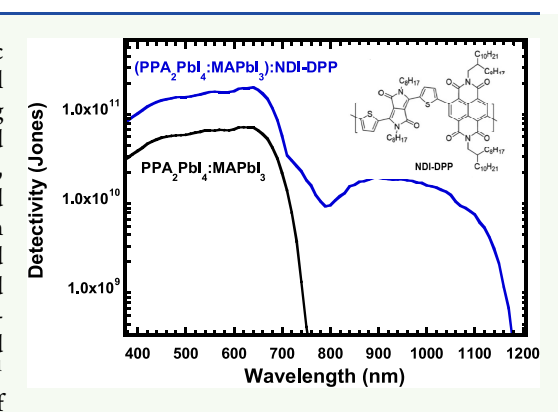
Cite This: https://doi.org/10.1021/acsaelm.4c00622



ACCESS |

Metrics & More

ABSTRACT: Broadband photodetectors have been used in various scientific and industrial sectors. Studies indicated that hybrid organic—inorganic metal halide perovskites (MHPs) are one of the semiconductors used for approaching sensitive photodetectors. Here, we reported solution-processed broadband photodetectors based on the ternary MHPs-conjugated polymer composites, which are operated at room temperature, where the ternary MHPs-conjugated polymer composites are composed of three-dimensional MHPs mixed with two-dimensional MHPs and then incorporated with low bandgap conjugated polymer. The ternary MHPs-conjugated polymer composites possess enhanced charge carrier mobility and suppressed defects. As a result, the ternary MHPs-conjugated polymer photodetectors exhibit a broad photoresponse, boosted photocurrent, and suppressed dark current, resulting in a detectivity of $\sim 10^{11}$ cm $\rm Hz^{1/2}~W^{-1}$ (jones) from the ultraviolet to visible region and a detectivity of



Article Recommendations

 $\sim 10^{10}$ jones in the near-infrared region. Our studies indicate that we provide a simple way to approach broadband photodetectors based on the ternary MHPs-conjugated polymer composites.

KEYWORDS: metal halide perovskites, 2D mixed 3D perovskite composites, ternary perovskite-conjugated polymer composites, photodetectors, broadband photoresponse

1. INTRODUCTION

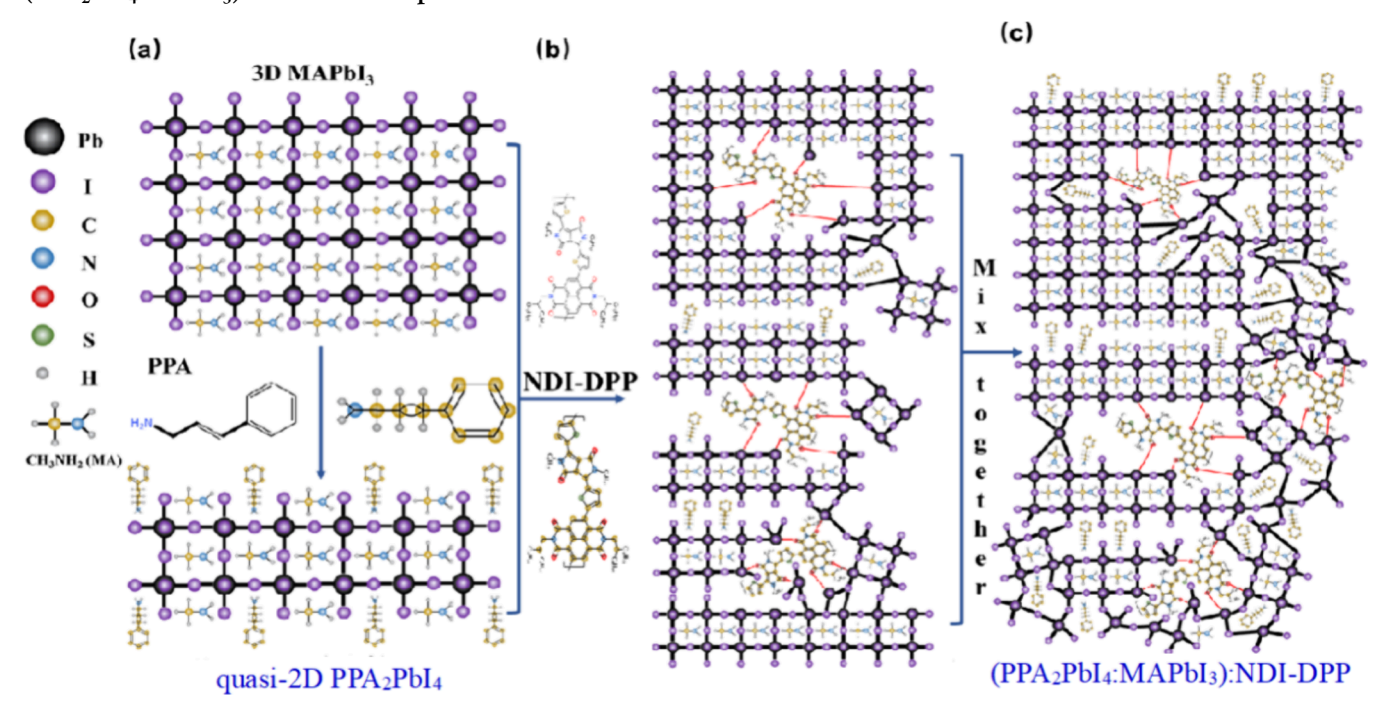
Photodetectors (PDs), which convert the optical signal into electricity, have great applications in optical fiber communication, imaging sensors, environmental monitoring, day/night surveillance, remote control, etc. 1-3 Studies indicated that hybrid organic-inorganic metal halide perovskites (MHPs) are one of the photovoltaic materials used for approaching ultrasensitive PDs. Compared to traditional semiconductor materials, such as silicon, germanium, gallium nitride, indium gallium arsenic, and semiconducting organic molecules/ polymers, 4-7 MHPs possess advanced features such as strong absorption coefficients, long carrier transmission distances, and adjustable direct bandgaps. Studies demonstrated that the PDs based on MHPs can maintain high sensitivity and detectability at room temperature (RT).8-17 In 2014, Xie et al. first reported MHP-based PDs. 12 In early 2015, we independently reported ultrasensitive MHP-based PDs through the utilization of fullerene derivatives as a passivation layer. 13 Since then, the research boom of MHP-based PDs has been initiated, especially the PDs based on the three-dimensional (3D) MHPs, for example, 3D MAPbI₃ (MA⁺:CH₃NH₃⁺), have made great progress. However, studies demonstrated that 3D MHPs are sensitive to water and oxygen, leading to dramatic degradation in an ambient atmosphere. Formation of lowdimensional layered MHPs by replacing organic small molecules (e.g., MA⁺) with organic macromolecules (e.g., C₈H₉NH³⁺, PEA⁺) with larger spatial site resistance is an effective method to enhance MHPs stability. However, the insulating organic cation-based low-dimensional layered MHPs possess poor charge transport due to the intrinsic features of the insulating organic cations. To circumvent these problems, we developed the two-dimensional (2D) MHPs created by conjugated organic molecule cation, aniline, and 3-phenyl-2-propen-1-amine (PPA) (Scheme 1a), and further found that the 3D MAPbI₃ incorporated with 2D PPA₂PbI₄ exhibited boosted charge transport. Thus, solar cells based on the 3D MAPbI₃ incorporated with the 2D PPA₂PbI₄ exhibited enhanced stability and photocurrent compared to those based on the 3D MHPs. ¹⁹

Moreover, due to the quantum confinement effect and the generated electroluminescence generated in the low-energygap region, increased exciton binding energy could induce lowdimensional layered MHPs to possess high carrier complex-

Received: April 9, 2024 Revised: April 23, 2024 Accepted: April 26, 2024



Scheme 1. Schematic Illustrations of (a) 3D MAPbI₃ and Quasi-2D PPA₂PbI₄, (b) Quasi-2D PPA₂PbI₄ Mixed with 3D MAPbI₃ (2D:3D PPA₂PbI₄:MAPbI₃) Composites, and (c) 2D:3D Mixed MHPs Incorporating NDI-DPP Ternary (PPA₂PbI₄:MAPbI₃):NDI-DPP Composites^a



^aThe molecular structures of PPA and NDI-DPP are presented in (a) and (b), respectively.

ation chances in the vertical direction, which greatly restricts device performance, such as responsivity and detectivity of MHP-based PDs. ¹⁸ In addition, the large dielectric constant of low-dimensional MHPs due to the introduction of macromolecular ligands makes the forbidden bandwidth of low-dimensional MHPs much larger than that of 3D MHPs (>1.51 eV), and the absorption wavelength is below 820 nm, without the near-infrared (NIR) spectral response, thereby severely limiting their IR detection applications, especially in biomedical imaging.

Conjugated organic molecules/polymers have the advantages of adjustable bandgap, solution processing, large-area processing, mechanical flexibility, lightweight, and low cost. It was found that MHPs incorporated with semiconducting organic molecules/polymers with the NIR absorption to construct the PDs with bilayer binary heterojunctions can compensate for the difficulty of extending the detection range of PDs to the NIR region. The construction of bilayer binary heterojunctions by introducing an organic native heterojunction as the second absorber layer has been shown to accelerate the rate of exciton dissociation, resulting in a boosted photocurrent and an extended photoresponse. 21-25 For example, we reported broadband PDs based on the 3D MHPs incorporated with low bandgap conjugated polymers.²² Li's group reported UV-visible-near-infrared photodetectors through utilization of a 3D MHPs/low bandgap conjugated polymers bilayer thin film structure.^{23,25}

Through harvesting the NIR absorption from low bandgap conjugated organic molecules, we reported efficient ternary MHPs—organic solar cells. In this ternary MHPs—organic composite, the 2D MHPs were first created by using a conjugated organic cation, 4-fluorobenzylammonium (4F-BEA), and then 4F-BEA-based 2D MHPs mixed with its corresponding 3D MHPs to make 2D mixed 3D (2D:3D)

MHPs composites. After that, the 2D:3D mixed MHPs were further incorporated with low bandgap conjugated organic molecules, O6T-4F, to form ternary MHPs—organic composites. It was found that ternary MHPs—organic composites possessed a broad absorption ranging from 350 to 1050 nm, superior film morphology, enhanced crystallinity, balanced charge transport, and effective photoinduced charge transfer. As a result, the ternary MHPs—organic solar cells exhibited a power conversion efficiency (PCE) of 23.60% compared to a PCE of 15.72% observed from solar cells based on the 3D MHPs.²⁶ Therefore, the strategy of constructing novel ternary MHPs—organic composite thin films by introducing low bandgap conjugated polymers is expected to lead to PDs with high sensitivity and broadband detection.

In this study, solution-processed ternary MHPs-conjugated polymer PDs with a broadband photoresponse up to 1200 nm are reported. The ternary MHPs-conjugated polymer composites are composed of p-type 2D:3D PPA₂PbI₄:MAPbI₃ composites mixed with n-type low bandgap semiconducting polymer, poly[(N,N'-bis(2-octyldodecyl)-1,4,5,8-naphthalene diimide-2,6-diyl)(2,5-dioctyl-3,6-di(thiophen-2-yl)pyrrolo[3,4-c]pyrrole-1,4-dione-5,5'-diyl)] (NDI-DPP, Scheme 1b)²² and 2D:3D PPA₂PbI₄:MAPbI₃):NDI-DPP, Scheme 1c). It is found that the ternary MHPs-conjugated polymer composites possess balanced charge transport and suppressed defects. As a result, at RT, the ternary MHPs-conjugated polymer PDs exhibit a photoresponse ranging from 370 to 1200 nm, a detectivity of ~10¹¹ cm Hz^{1/2} W⁻¹ (jones) in the UV-visible region, and a detectivity of ~10¹⁰ jones in the NIR region.

2. RESULTS AND DISCUSSION

Scheme 1 schematically illustrates 3D MAPbI₃, quasi-2D PPA₂PbI₄, and quasi-2D PPA₂PbI₄ mixed with 3D MAPbI₃

ACS Applied Electronic Materials

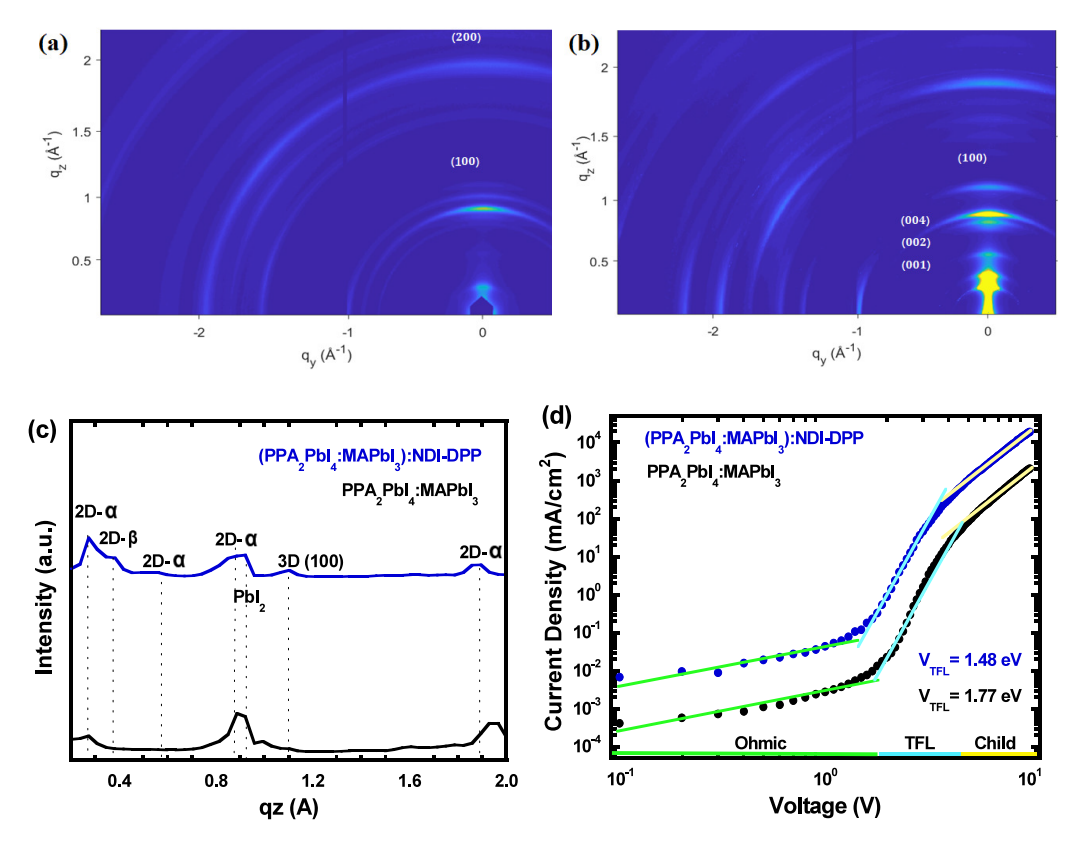


Figure 1. 2D GIWAXS profiles of (a) PPA₂PbI₄:MAPbI₃ and (b) (PPA₂PbI₄:MAPbI₃):NDI-DPP thin films. (c) 1D GIWAXS in the out-of-plane direction for PPA₂PbI₄:MAPbI₃ and (PPA₂PbI₄:MAPbI₃):NDI-DPP thin films. (d) Electron-only diodes made by either PPA₂PbI₄:MAPbI₃ or (PPA₂PbI₄:MAPbI₃):NDI-DPP thin films.

(PPA₂PbI₄:MAPbI₃) composites. Both 3D MAPbI₃ and quasi-2D PPA₂PbI₄ are p-type semiconductors; thus, the 2D:3D PPA₂PbI₄:MAPbI₃ composites are also p-type semiconductors. To balance charge transport and extend absorption up to the NIR region, n-type, the low bandgap gap conjugated polymer, NDI-DPP²² (see molecular structure in Scheme 1b), is mixed with PPA₂PbI₄:MAPbI₃ composites, which leads to the formation of ternary (PPA₂PbI₄:MAPbI₃):NDI-DPP composites. Scheme 1c illustrates the formation of the (PPA₂PbI₄:MAPbI₃):NDI-DPP composites. NDI-DPP is selected as the electron acceptor since it displays high electron mobility, which is anticipated to balance charge transport and facilitate exciton dissociation within the ternary composites.

The grazing-incidence wide-angle X-ray scattering (GI-WAXS) is first performed for verifying the crystal structures of PPA₂PbI₄:MAPbI₃ and (PPA₂PbI₄:MAPbI₃):NDI-DPP composite thin films. Figure 1a-c displays the GIWAXS profiles of the PPA₂PbI₄:MAPbI₃ and (PPA₂PbI₄:MAPbI₃):NDI-DPP composite thin films. The same as the 3D MAPbI₃ thin film, both PPA₂PbI₄:MAPbI₃ and (PPA₂PbI₄:MAPbI₃):NDI-DPP composites possess tetragonal crystal structure. However, in addition to the diffraction rings for the 3D MAPbI₃ thin film, the diffraction arch at $q_r =$ 0.4, which corresponds to the (001) plane of the 2D PPA₂PbI₄ phase, is visible in the PPA2PbI4:MAPbI3 composite thin film.27 Moreover, with NDI-DPP mixed with the PPA₂PbI₄:MAPbI₃, the (PPA₂PbI₄:MAPbI₃):NDI-DPP thin film possesses diffraction peaks in the 2D- α and 2D- β phases (Figure 1a-c), indicating that NDI-DPP could induce the PPA₂PbI₄:MAPbI₃ composite thin film to grow along the vertical direction. Thus, compared to the PPA2PbI4:MAPbI3 thin film, the (PPA₂PbI₄:MAPbI₃):NDI-DPP thin film is anticipated to have enhanced charge carrier mobility.²⁸

To verify the above hypothesis, the electron mobilities of both PPA₂PbI₄:MAPbI₃ and (PPA₂PbI₄:MAPbI₃):NDI-DPP thin films are studied according to the space charge limited current (SCLC) method, which is based on the Mott-Gurney model.^{29,30} The electron mobility (μ_e) is described as J = $(9\varepsilon\varepsilon_0\mu v^2)/(8L^3)$, where *J* is the current density, *V* is the external bias, L is the thickness of the active layer, ε_0 is the vacuum permittivity (8.55 \times 10⁻¹² F m⁻¹), and ε is the relative dielectric constant for the active layer. Based on the current density versus voltage (J-V) characteristics, as shown in Figure 1d, from the electron-only diodes with a device architecture of ITO/SnO₂/MHPs/PC₆₁BM/Ag (where ITO is indium tin oxides, SnO₂ is tin oxide, PC₆₁BM is phenyl-C₆₁-butyric acid methyl ester, and Ag is sliver), the electron mobilities of the PPA₂PbI₄:MAPbI₃ and (PPA₂PbI₄:MAPbI₃):NDI-DPP thin films are evaluated to be $\sim 2.1 \times 10^{-4}$ and $\sim 9.4 \times 10^{-4}$ cm² V⁻¹ s⁻¹, respectively. Thus, compared to the PPA₂PbI₄:MAPbI₃ thin film, the electron mobility of the (PPA2PbI4:MAPbI3):NDI-DPP thin film is enhanced approximately 5 times. These results confirm that NDI-DPP could indeed tune the orientation of MHPs, resulting in a boosted electron mobility.

The UV—vis absorption spectra of the PPA₂PbI₄:MAPbI₃, NDI-DPP, and (PPA₂PbI₄:MAPbI₃):NDI-DPP thin films are shown in Figure 2a. The absorption of the PPA₂PbI₄:MAPbI₃ thin film ranges from 370 to 780 nm, which is consistent with other reports.³¹ The absorption of the NDI-DPP thin film ranges from 300 to 1200 nm, which is consistent with our previous studies,²² whereas the absorption of the

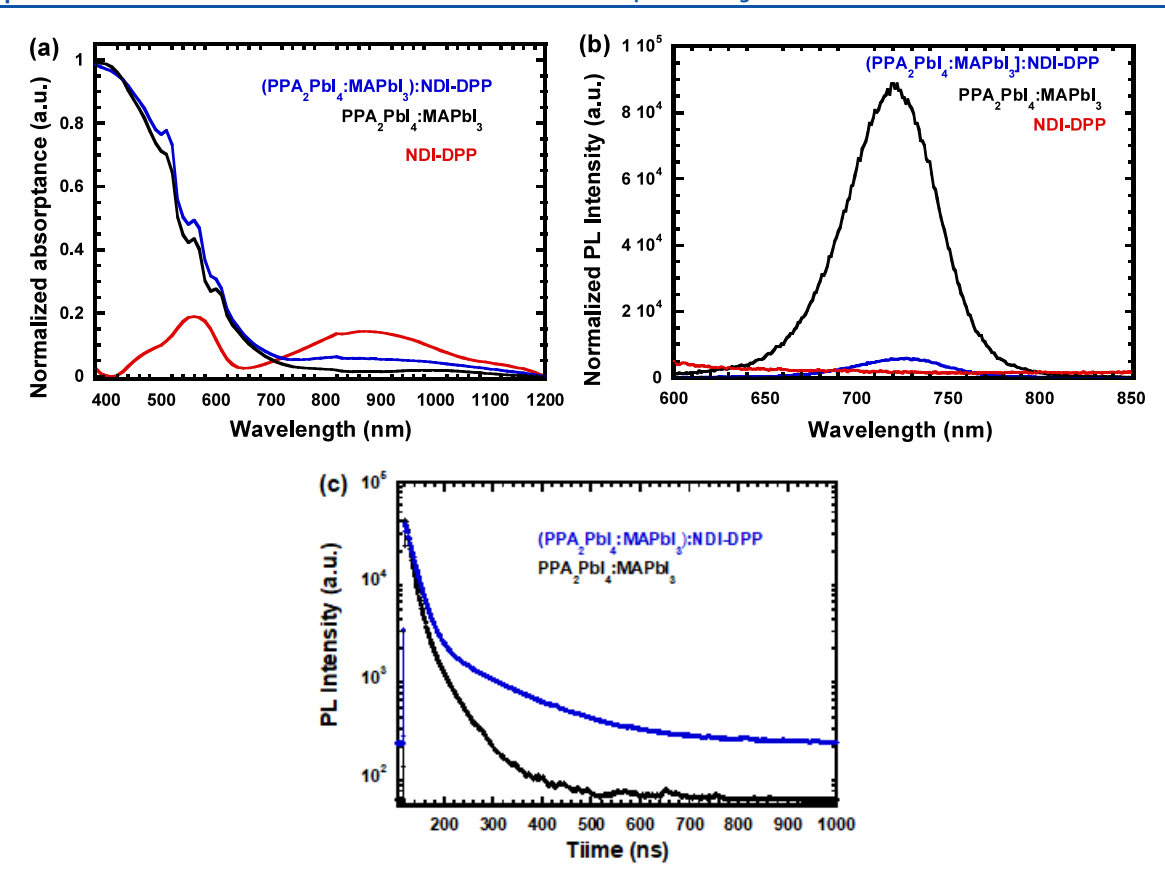
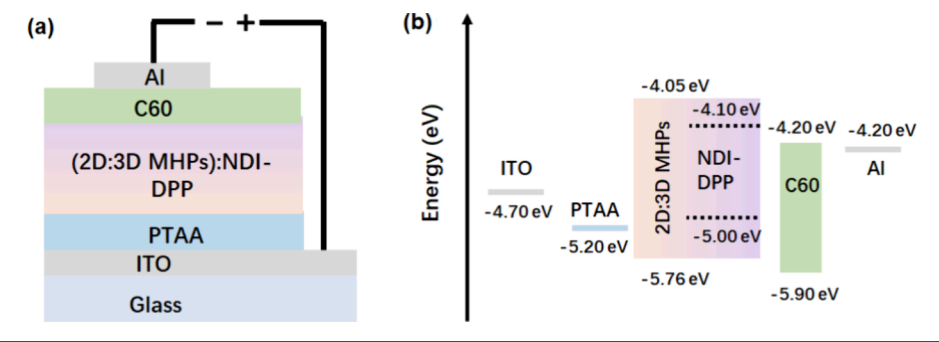


Figure 2. (a) Absorption and (b) photoluminescent (PL) spectra of PPA₂PbI₄:MAPbI₃, (PPA₂PbI₄:MAPbI₃):NDI-DPP, and NDI-DPP thin films. (c) Time-resolved PL (TR-PL) spectra of PPA₂PbI₄:MAPbI₃ and (PPA₂PbI₄:MAPbI₃):NDI-DPP thin films.

Scheme 2. (a) Device Structure of Ternary MHPs-Conjugated Polymer Photodetectors, (b) LUMO and HOMO Energy Levels of 2D:3D Mixed MHPs, NDI-DPP, PTAA, and C_{60} , and Work Functions of the ITO and Al Electrodes



(PPA₂PbI₄:MAPbI₃):NDI-DPP thin film is the superposition of both PPA₂PbI₄:MAPbI₃ and NDI-DPP thin films, ranging from 370 to 1200 nm.

Figure 2b displays the steady-state photoluminescence (PL) spectra of the (PPA₂PbI₄:MAPbI₃):NDI-DPP thin films and the (PPA₂PbI₄:MAPbI₃):NDI-DPP thin films. Under an excitation wavelength of 500 nm, the PPA₂PbI₄:MAPbI₃ thin film exhibits a strong emission peak at 730 nm. Under the same photoexcitation, the NDI-DPP thin film exhibits no emission. However, as compared to the PPA₂PbI₄:MAPbI₃ thin film, the PL intensity of the (PPA₂PbI₄:MAPbI₃):NDI-DPP thin film is dramatically quenched, which indicates that the effective photoinduced charge transfer rather than nonradiative charge recombination plays a crucial role in the ternary MHPs-polymer composites, (PPA₂PbI₄:MA-PbI₃):NDI-DPP.²⁶

The time-resolved PL (TR-PL) is investigated to understand the charge carrier recombination behavior and charge carrier dynamics in both PPA2PbI4:MAPbI3 and (PPA₂PbI₄:MAPbI₃):NDI-DPP thin films. Figure 2c presents the TR-PL results of both the PPA₂PbI₄:MAPbI₃ and (PPA₂PbI₄:MAPbI₃):NDI-DPP thin films. Under the same excitation wavelength, the PPA2PbI4:MAPbI3 thin film exhibits a short decay lifetime, whereas the (PPA₂PbI₄:MAPbI₃):NDI-DPP thin film exhibits a much longer transient lifetime. Specifically, a lifetime of a few hundred picoseconds is observed from the PPA₂PbI₄:MAPbI₃ composite thin film, while the signal of a few nanoseconds is observed from the (PPA2PbI4:MAPbI3):NDI-DPP composite thin film. A longer transient lifetime reveals the presence of longer-lived charge carriers in the (PPA₂PbI₄:MAPbI₃):NDI-DPP.³² Therefore, efficient photoinduced charge transfer occurs within the **ACS Applied Electronic Materials**

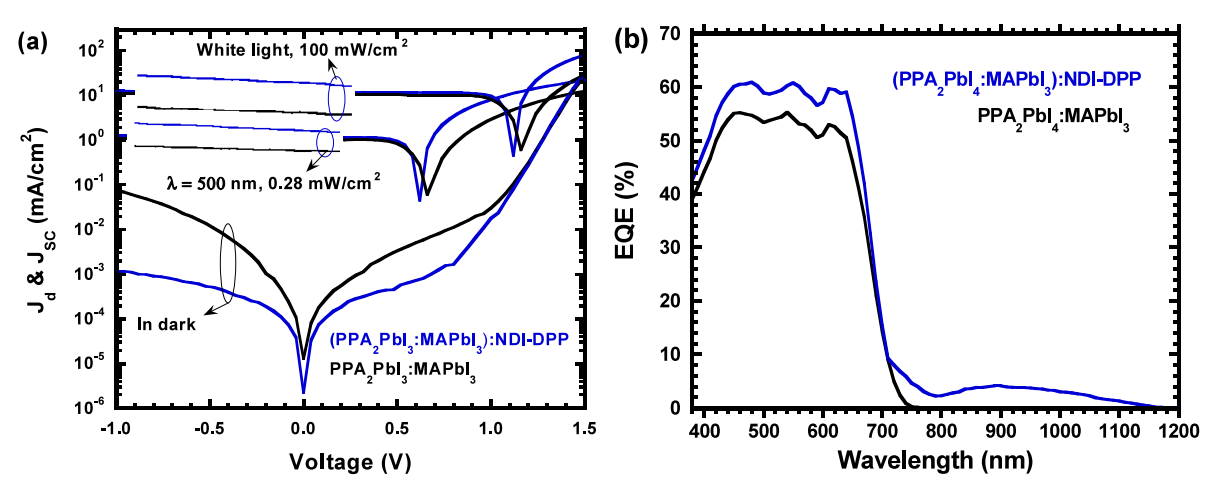


Figure 3. (a) J-V characteristics and (b) EQE spectra of the photodetectors based on either PPA₂PbI₄:MAPbI₃ or (PPA₂PbI₄:MAPbI₃):NDI-DPP thin films.

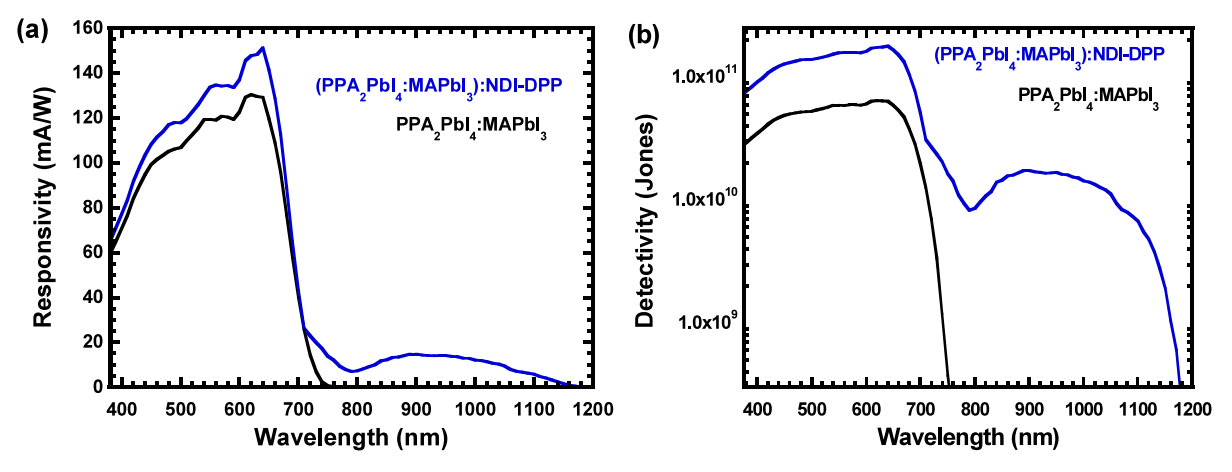


Figure 4. (a) Responsivity and (b) detectivity of the photodetectors based on either PPA₂PbI₄:MAPbI₃ or (PPA₂PbI₄:MAPbI₃):NDI-DPP thin films.

 $(PPA_2PbI_4:MAPbI_3):NDI-DPP$ composite thin film. As a result, a boosted photocurrent is expected to be observed from the PDs based on the $(PPA_2PbI_4:MAPbI_3):NDI-DPP$ thin film.

The device structure of ternary MHPs-polymer PDs is shown in Scheme 2a. The photoactive layer is either PPA₂PbI₄:MAPbI₃ or (PPA₂PbI₄:MAPbI₃):NDI-DPP composite single-layer thin films. Scheme 2b illustrates the schematic of both the lowest unoccupied molecular orbit (LUMO) and the highest occupied molecular orbit (HOMO) energy levels of the PTAA hole extraction layer (HEL), the C₆₀ electron extraction layer (EEL), PPA2PbI4:MAPbI3, and NDI-DPP and the work functions of ITO and Al electrodes. The matched energy levels of the PPA2PbI4:MAPbI3 layer with the PTAA HEL and the ITO anode and the C₆₀ EEL and the Al cathode can ensure efficient carrier extraction and collection. 18,19,22,26,33,34 Moreover, the LUMO energy levels offset between the PPA2PbI4:MAPbI3 and NDI-DPP could ensure photoinduced charge transfer from the PPA2PbI4:MAPbI3 to NDI-DPP, which is consistent with the quenched PL observed from the (PPA₂PbI₄:MAPbI₃):NDI-DPP composites. Therefore, the PDs based on the (PPA2PbI4:MAPbI3):NDI-DPP composite thin film are expected to have a broad photoresponse and a boosted photocurrent.

The J-V characteristics of the PDs fabricated by either PPA₂PbI₄:MAPbI₃ or (PPA₂PbI₄:MAPbI₃):NDI-DPP composite thin films measured in the dark and under white light with a light intensity of 100 mW/cm² and a monochromatic light at the wavelength (λ) of 500 nm with a light intensity of 0.28 mW/cm² and biased at -0.2 V are shown in Figure 3a. At RT and under white light illumination with a light intensity of 100 mW/cm², the photocurrent density of 10.56 mA/cm² is observed from the PDs fabricated by the PPA2PbI4:MAPbI3 thin film, whereas the PDs fabricated by the (PPA2PbI4:MAPbI3):NDI-DPP thin film exhibit a photocurrent density of 12.10 mA/cm². Moreover, under a monochromatic light at λ of 500 nm with a light intensity of 0.28 mW/cm^2 and biased at -0.2 V, the photocurrent density of 1.04 mA/cm² is observed from the PDs fabricated by the PPA₂PbI₄:MAPbI₃ composite thin film, whereas the PDs fabricated by the (PPA₂PbI₄:MAPbI₃):NDI-DPP composite thin film exhibit a photocurrent density of 1.20 mA/cm². These results indicate that the PDs fabricated by the (PPA₂PbI₄:MAPbI₃):NDI-DPP thin film have a boosted photocurrent compared to that based on the PPA2PbI4:MAPbI3 thin film. On the other hand, the PDs fabricated by the (PPA2PbI4:MAPbI3):NDI-DPP thin film possess a dark current density of 2.23×10^{-6} A/cm², which is nearly 6 times lower than that $(1.28 \times 10^{-5} \text{ A/cm}^2)$ observed

from the PDs fabricated by the PPA2PbI4:MAPbI3 composite thin film. Such suppressed dark current density is probably ascribed to a better film morphology of the (PPA2PbI4:MAPbI3):NDI-DPP composites. Moreover, as indicated in Figure 1d, the trap-filling limiting voltage ($V_{\rm TFL}$) of the PDs fabricated by the (PPA2PbI4:MAPbI3):NDI-DPP composite thin film is reduced to 1.48 V from 1.77 V for the PDs fabricated by the PPA2PbI4:MAPbI3 composite thin film. A smaller $V_{\rm TFL}$ indicates that the defect within the (PPA2PbI4:MAPbI3):NDI-DPP composite thin film is suppressed compared to that of the PPA2PbI4:MAPbI3 composite thin film. As a result, the PDs fabricated by the (PPA2PbI4:MAPbI3):NDI-DPP composite thin film possess a suppressed dark current density.

The external quantum efficiency (EQE) spectra of the PDs fabricated by either PPA2PbI4:MAPbI3 or (PPA2PbI4:MAPbI3):NDI-DPP composite thin films are shown in Figure 3b. The EQE spectrum of the PDs based on the PPA₂PbI₄:MAPbI₃ composite thin film ranges from 370 to 750 nm, which is in good agreement with the absorption spectrum of the PPA2PbI4:MAPbI3 composite thin film, whereas the EQE spectrum of the PDs based on the (PPA₂PbI₄:MAPbI₃):NDI-DPP thin film ranges from 370 to 1200 nm, which is consistent with the absorption spectrum of the (PPA₂PbI₄:MAPbI₃):NDI-DPP composite thin film. Moreover, the PDs based on the (PPA2PbI4:MAPbI3):NDI-DPP composite thin film possesses enhanced EQE values compared to that by the PPA2PbI4:MAPbI3 composite thin film from 420 to 650 nm. Such enhanced EQE values are ascribed to the ordered phase distribution to form a gradient of the PPA₂PbI₄:MAPbI₃ thin film (Figure 1a-c), which provides an excellent charge transport channel, resulting in a boosted photocurrent.

The responsivity (R), which is described as $R = I_{\rm L}/I_{\rm Light}$ (where $I_{\rm L}$ is photocurrent and $I_{\rm Light}$ is the light intensity), 35 is used to characterize the ability of a PD to detect an optical signal. Based on the EQE spectra of PDs, the R values versus wavelength are shown in Figure 4a. The PDs based on the PPA₂PbI₄:MAPbI₃ composite thin film exhibit a spectral response from 370 to 760 nm, whereas the PDs based on the (PPA₂PbI₄:MAPbI₃):NDI-DPP composite thin film exhibit a spectral response from 370 to 1200 nm. Moreover, similar to the EQE spectra, the PDs based on the (PPA₂PbI₄:MAPbI₃):NDI-DPP composite thin film possesses boosted R values from 370 to 660 nm compared to that based on the PPA₂PbI₄:MAPbI₃ composite thin film.

The specific detectivity (D^*) is one of the key parameters used to evaluate the device performance of PDs. D^* is described as

$$D^* = \frac{R}{\sqrt{2qI_D}}$$

where R is responsivity, q is element charge, and $I_{\rm D}$ is dark current. Typically, the $I_{\rm D}$ is considered to be the main factor in the noise signal, and other noise is considered to be negligible. The lower the $I_{\rm D}$, the higher the D^* can be achieved. The D^* values versus wavelengths are shown in Figure 4b. For both PDs, the peak detection is at the same wavelength, which is 640 nm. But the PDs based on the $(PPA_2PbI_4:MAPbI_3):NDI-DPP$ composite thin film possesses a broadband spectral detection from 370 to 1200 nm. Moreover, the PDs fabricated by the

(PPA₂PbI₄:MAPbI₃):NDI-DPP thin film exhibits a D^* of 1.78×10^{11} jones, which is approximately 3 times higher than that (6.53 \times 10¹⁰ jones) based on the PPA₂PbI₄:MAPbI₃ composite thin film. In addition, the PDs fabricated by the (PPA₂PbI₄:MAPbI₃):NDI-DPP composite thin film possess a D^* of 10^{10} jones in the NIR region.

3. CONCLUSIONS

In this study, room-temperature-operated solution-processed broadband photodetectors based on metal halide perovskites (MHPs) incorporated with a low bandgap conjugated polymer (NDI-DPP), which exhibited a photoresponse from 370 to 1200 nm, were reported. The MHPs-conjugated polymer composites were composed of 3D:2D MHPs incorporated with low bandgap conjugated polymer composites, where the 2D MHPs were based on conjugated organic cation. Studies indicated that the ternary MHPs-conjugated polymer composites possessed enhanced charge carrier mobility and suppressed defects. As a result, the ternary MHPs-conjugated polymer photodetectors possessed an extended spectral response up to 1200 nm. Moreover, the ternary MHPsconjugated polymer photodetectors exhibited a projected detectivity of 1011 jones, which was three times higher than that by the 2D:3D mixed MHPs composite thin film. The results reported in this study indicated that we realized a simple way to approach broadband photodetectors based on the ternary MHPs-conjugated polymer composites.

4. EXPERIMENTAL SECTION

- **4.1. Materials.** Lead iodide (PbI₂, 99.999%), hydroiodic acid (HCl, 37%), methylammonium acetate (MAAc), and methylamine (CH₃NH₂, 40 wt % in H₂O) were purchased from Sigma-Aldrich. Hydroiodic acid and methylamine were used to synthesize methylammonium iodide (CH₃NH₃I (MAI)) according to a previous report. Poly[bis(4-phenyl)(2,4,6-trimethylphenyl)amine (PTAA) and fullerene C60 were purchased from Sigma-Aldrich and Solenne BV, respectively. Anhydrous N,N-dimethylformamide (DMF, 99.8%), anhydrous ethanol (>99.5%), anhydrous toluene (99.8%), and anhydrous chlorobenzene (CB, 99.8%) were purchased from Sigma-Aldrich. All materials were used as received without further purification.
- **4.2. Thin Film Characterization.** Thin film thickness was performed by a surface profilometer. The absorption spectra of thin films were characterized with a commercially available spectrophotometer (PerkinElmer, Waltham, MA). The molecular packing patterns of the thin films were characterized by the GIWAXS system (Beamline 8-ID-E, APS, Argonne National Laboratory). The details of thin film characterization can be found in our previous publications. ^{13,19,20}
- **4.3. Photodetector Fabrication and Characterization.** Precleaned indium tin oxide (ITO) (15 Ω \Box^{-1}) substrates or glass substrates were treated with ultraviolet (UV)-ozone for 30 min. For the devices, a PTAA film was deposited by spin-coating at 5000 rpm for 30 s on the cleaned conductive glass substrates and then dried at 100 °C for 10 min in ambient air. The photoactive layers were fabricated in an N_2 glovebox. Then, the C_{60} solution (20 mg/mL in chlorobenzene) was spin-coated onto the photoactive layers at 1500 rpm for 50 s. Finally, a 20 nm C_{60} and a 100 nm aluminum (Al) electrode are thermally deposited through a shadow mask in the vacuum with a press of 1×10^{-6} mbar. The active device area is measured to be 0.043 cm². All devices were not encapsulated.

The J-V characteristics of photodetectors were performed on a Keithley model 2400 source measure unit in dark and white light with the light intensity of 100 mW cm⁻² and monochromatic light at a wavelength (λ) of 500 nm with the light intensities of 0.28 mW cm⁻² and biased at 0.2 V. The external quantum efficiency (EQE) spectra

of photodetectors were obtained by using the solar cell quantum efficiency measurement system (QEX10) from PV measurements with a 300 W steady-state xenon lamp as the source light.

The details of photodetector fabrication and characterization can be found in our previous publications. 13,19,26,33,34

AUTHOR INFORMATION

Corresponding Authors

Tao Zhu — School of Polymer Science and Polymer Engineering, College of Engineering and Polymer Science, The University of Akron, Akron, Ohio 44325, United States; orcid.org/0000-0001-9614-3476; Email: zhutao3306@

Xiong Gong — School of Polymer Science and Polymer Engineering, College of Engineering and Polymer Science, The University of Akron, Akron, Ohio 44325, United States; orcid.org/0000-0001-6525-3824; Email: xgong@uakron.edu

Authors

Lening Shen — School of Polymer Science and Polymer Engineering, College of Engineering and Polymer Science, The University of Akron, Akron, Ohio 44325, United States

Xiyao Zhang — School of Polymer Science and Polymer Engineering, College of Engineering and Polymer Science, The University of Akron, Akron, Ohio 44325, United States

Lei Liu – School of Polymer Science and Polymer Engineering, College of Engineering and Polymer Science, The University of Akron, Akron, Ohio 44325, United States

Hussain Sawwan – School of Polymer Science and Polymer Engineering, College of Engineering and Polymer Science, The University of Akron, Akron, Ohio 44325, United States

Complete contact information is available at: https://pubs.acs.org/10.1021/acsaelm.4c00622

Author Contributions

L.S. and X.Z. equally contributed to this work.

Notes

The authors declare no competing financial interest.

ACKNOWLEDGMENTS

The authors acknowledge the National Science Foundation (ECCS/EPMD1903303) for financial support.

REFERENCES

- (1) Jha, A. R. Infrared Technology; John Wiley & Sons, Inc.: 2000.
- (2) Cao, G. R.; Liu, L. S.; Li, L. Short-Wave Infrared Photodetector. *Mater. Today* **2023**, *62*, 327–349.
- (3) García de Arquer, F. P.; Armin, A.; Meredith, P.; Sargent, E. H. Solution-Processed Semiconductors for Next-Generation Photodetectors. *Nat. Rev. Mater.* **2017**, *2*, 1–17.
- (4) Wu, Z.; Zhai, Y.; Kim, H.; Azoulay, J. D.; Ng, T. N. Emerging Design and Characterization Guidelines for Polymer-Based Infrared photodetectors. *Acc. Chem. Res.* **2018**, *51*, 3144–3153.
- (5) Liu, X.; Lin, Y.; Liao, Y.; Wu, J.; Zheng, Y. Recent Advances in Organic Near-Infrared Photodiodes. *J. Mater. Chem. C* **2018**, *6*, 3499–3513.
- (6) Li, G. X.; Wang, Y. K.; Huang, L. X.; Sun, W. H. Research Progress of High-Sensitivity Perovskite Photodetectors: A Review of Photodetectors: Noise, Structure, and Materials. *ACS Appl. Electron. Mater.* **2022**, *4*, 1485–1505.
- (7) Lu, X.; Li, J.; Zhang, Y.; Han, Z.; He, Z.; Zou, Y.; Xu, X. Recent Progress on Perovskite Photodetectors for Narrowband Detection. *Adv. Photonics Res.* **2022**, *3*, 2100335.

- (8) Kojima, A.; Teshima, K.; Shirai, Y.; Miyasaka, T. Organometal Halide Perovskites as Visible-Light Sensitizers for Photovoltaic Cells. *J. Am. Chem. Soc.* **2009**, *131*, 6050–6051.
- (9) Xing, G. C.; Mathews, N.; Sun, S. Y.; Lim, S. S.; Lam, Y. M.; Grätzel, M.; Mhaisalkar, S.; Sum, T. C. Long-Range Balanced Electron- and Hole-Transport Lengths in Organic-Inorganic CH₃NH₃PbI₃. Science **2013**, 342, 344–347.
- (10) Burschka, J.; Pellet, N.; Moon, S. J.; Humphry-Baker, R.; Gao, P.; Nazeeruddin, M. K.; Grätzel, M. Sequential Deposition As A Route to High-Performance Perovskite-Sensitized Solar Cells. *Nature* **2013**, 499, 316–319.
- (11) Wang, C.; Zhang, X. T.; Hu, W. P. Organic Photodiodes and Phototransistors Toward Infrared Detection: Materials, Devices, and Applications. *Chem. Soc. Rev.* **2020**, *49*, 653–670.
- (12) Hu, X.; Zhang, X.; Liang, L.; Bao, J.; Li, S.; Yang, W. L.; Xie, Y. High-Performance Flexible Broadband Photodetector Based on Organolead Halide Perovskite. *Adv. Funct. Mater.* **2014**, *24*, 7373–7380
- (13) Liu, C.; Wang, K.; Yi, C.; Shi, X.; Du, P.; Smith, A. W.; Karim, A.; Gong, X. Ultrasensitive Solution-Processed Perovskite Hybrid Photodetectors. *J. Mater. Chem. C* **2015**, *3*, 6600–6606.
- (14) Pan, X. Y.; Ding, L. M. Application of Metal Halide Perovskite Photodetectors. *J. Semicond.* **2022**, *43*, 020203.
- (15) Sun, J.; Ding, L. M. A Polarization-Sensitive Photodetector with Patterned CH₃NH₃PbCl₃ film. *Small* **2024**, *20*, 2308583.
- (16) Li, L.; Chen, H.; Fang, Z.; Meng, X.; Zuo, C.; Lv, M.; Tian, Y.; Fang, Y.; Xiao, Z.; Shan, C.; Xiao, Z.; Jin, Z.; Shen, G.; Shen, L.; Ding, L. An Electrically Modulated Single-Color/Dual-Color Imaging Photodetector. *Adv. Mater.* **2020**, *32*, 1907257.
- (17) Zhang, J. J.; Pan, X. Y.; Sun, J.; Zhou, H.; Zhang, G. P.; Ding, L. M. A-site Cation Exchange Enables a High-Performance CsPbBr₃ Photodetector for Laser Eavesdropping Systems. *Adv. Optical Mater.* **2024**, *12*, 2302848.
- (18) Zhu, T.; Gong, X. Low-Dimensional Perovskite Materials and Their Optoelectronics. *InfoMat* **2021**, *3*, 1039–1069.
- (19) Zhu, T.; Shen, L. N.; Chen, H. L.; Yang, Y. R.; Zheng, L. Y.; Chen, R.; Zheng, J.; Wang, J. P.; Gong, X. Conjugated Molecule Based 2D Perovskites for High-Performance Perovskite Solar Cells. J. Mater. Chem. A 2021, 9, 21910–21917.
- (20) Chen, S.; Teng, C.; Zhang, M.; Li, Y. R.; Xie, D.; Shi, G. A. A Flexible UV-Vis-NIR Photodetector Based on a Perovskite/Conjugated-Polymer Composite. *Adv. Mater.* **2016**, *28*, 5969–5974.
- (21) Zhang, Y.; Qin, Z.; Huo, X. M.; Song, D. D.; Qiao, B.; Zhao, S. L. High-Performance Near-Infrared Photodetectors Based on the Synergy Effect of Short Wavelength Light Filter and Long Wavelength Response of A Perovskite/Polymer Hybrid Structure. *ACS Appl. Mater. Interface* **2021**, *13*, 61818–61826.
- (22) Xu, W. Z.; Guo, Y.; Zhang, X. T.; Zheng, L. Y.; Zhu, T.; Zhao, D. H.; Hu, W. P.; Gong, X. Room-Temperature-Operated Ultrasensitive Broadband Photodetectors by Perovskite Incorporated with Conjugated Polymer and Single-Wall Carbon Nanotubes. *Adv. Funct. Mater.* **2018**, 28, 1705541.
- (23) Cao, F.; Tian, W.; Deng, K.; Wang, M.; Li, L. Self-Powered UV-Vis-NIR Photodetector Based on Conjugated-Polymer/CsPbBr₃ Nanowire Array. *Adv. Funct. Mater.* **2019**, 29, 1906756.
- (24) Wei, Y. Z.; Feng, G. T.; Mao, P.; Luan, Y. G.; Zhuang, J.; Chen, N. L.; Yang, H. X.; Li, W. W.; Yang, S. Y.; Wang, J. Z. Lateral Photodetectors Based on Double-Cable Polymer/Two-Dimensional Perovskite Heterojunction. ACS Appl. Mater. Interfaces 2020, 12 (7), 8826–8834.
- (25) Cao, F.; Wang, M.; Tian, W.; Sun, H. X.; Li, L. Stable, Semitransparent, and Self-Powered Conjugated-Polymer/CsPbI2Br UV-vis-NIR Photodetector Improved by Thiamine Additive. *Adv. Optical Mater.* **2022**, *10*, 2201579.
- (26) Zhu, T.; Shen, L. N.; Xun, S. N.; Sarmiento, J. S.; Yang, Y. R.; Zheng, L. Y.; Li, H.; Wang, H.; Bredas, J. L.; Gong, X. High-Performance Ternary Perovskite-Organic Solar Cells. *Adv. Mater.* **2022**, *34*, 2109348.

- (27) Wu, L. Y.; Li, G. X.; Prashanthan, K.; Musiienko, A.; Li, J. Z.; Gries, T. W.; Zhang, H.; Köbler, H.; Janasik, P.; Appiah, A. S.; Paramasivam, G.; Sun, T. X.; Li, M.; Marongiu, D.; Saba, M.; Abate, A. Stabilization of Inorganic Perovskite Solar Cells with a 2D Dion-Jacobson Passivating Layer. *Adv. Mater.* 2023, 35, 2304150.
- (28) Miao, Y.; Wu, J.; Qi, X.; Yang, L.; Wang, X.; Zheng, F.; Zhao, F.; Shafique, S.; Zhu, Y.; Hu, Z. Gradient 2D-3D Ruddlesden-Popper Perovskite Film for High-Performance Self-Powered Photodetectors. *Nano Energy* **2023**, *113*, 108605.
- (29) Bube, R. H. Trap Density Determination by Space Charge Limited Currents. J. Appl. Phys. 1962, 33, 1733-1737.
- (30) Le Corre, V. M.; Duijnstee, E. A.; El Tambouli, O.; Ball, J. M.; Snaith, H. J.; Lim, J.; Koster, L. J. A. Revealing Charge Carrier Mobility and Defect Densities in Metal Halide Perovskites via Space-Charge-Limited Current Measurements. ACS Energy Lett. 2021, 6, 1087
- (31) Fu, W. F.; Liu, H. B.; Shi, X. L.; Zuo, L. J.; Li, X. S.; Jen, A. K.-Y. Tailoring the Functionality of Organic Spacer Cations for Efficient and Stable Quasi-2D Perovskite Solar Cells. *Adv. Funct. Mater.* **2019**, 29, 1900221.
- (32) Zhou, M.; Sarmiento, J. S.; Fei, C. B.; Wang, H. Charge Transfer and Diffusion at the Perovskite/PCBM Interface Probed by Transient Absorption and Reflection. *J. Phys. Chem. C* **2019**, *123*, 22095.
- (33) Chen, H.; Teale, S.; Chen, B.; Hou, Y.; Grater, L.; Zhu, T.; Bertens, K.; Park, S. M.; Atapattu, H. R.; Gao, Y.; Wei, M.; Johnston, A. K.; Zhou, Q.; Xu, K.; Yu, D.; Han, C.; Cui, T.; Jung, E. H.; Zhou, C.; Zhou, W.; Proppe, A. H.; Hoogland, S.; Laquai, F.; Filleter, T.; Graham, K. R.; Ning, Z.; Sargent, E. H. Quantum-size-tuned heterostructures enable efficient and stable inverted perovskite solar cells. *Nat. Photonics* **2022**, *16*, 352–358.
- (34) Chen, R.; Shen, L. N.; Zheng, L. Y.; Zhu, T.; Liu, Y. H.; Liu, L.; Zheng, J.; Gong, X. Two-/Three-Dimensional Perovskite Bilayer Thin Films Post-Treated with Solvent Vapor for High-Performance Perovskite Photovoltaics. *ACS Appl. Mater. Interfaces* **2021**, 13, 49104–49113.
- (35) Gong, X.; Tong, M. H.; Xia, Y. J.; Cai, W. Z.; Moon, J. S.; Cao, Y.; Yu, G.; Shieh, C. L.; Nilsson, B.; Heeger, A. J. High-Detectivity Polymer Photodetectors with Spectral Response from 300 to 1450 nm. *Science* **2009**, 325, 1665–1667.
- (36) Tian, W.; Zhou, H.; Li, L. Hybrid Organic-Inorganic Perovskite Photodetectors. *Small* **2017**, *13*, 1702107.
- (37) Qiao, B. S.; Wang, S. Y.; Zhang, Z. H.; Lian, Z. D.; Zheng, Z. Y.; Wei, Z. P.; Li, L.; Ng, K. W.; Wang, S. P.; Liu, Z. B. Photosensitive Dielectric 2D Perovskite Based Photodetector for Dual Wavelength Demultiplexing. *Adv. Mater.* **2023**, 35, 2300632.
- (38) Zhang, X. Y.; Li, Z. Q.; Yan, T. T.; Su, L.; Fang, X. S. Phase-Modulated Multidimensional Perovskites for High-Sensitivity Self-Powered UV Photodetectors. *Small* **2023**, *19*, 2206310.
- (39) Wang, H.; Kim, D. H. Perovskite-Based Photodetectors: Materials and Devices. *Chem. Soc. Rev.* **2017**, *46*, 5204–5236.